ACS OMEGA

Open Access

http://pubs.acs.org/journal/acsodf

Article

Effects of Sodium Vacancies and Concentrations in Na_3SO_4F Solid Electrolyte

Xue Wang,[‖] Xuele Xu,[‖] Yuxiang Li, Wenqian Chen,* Guowei Zhao, Heng Wang, Ya Tang, Pengcheng Wu,* and Liang Tang*

Cite This: *ACS Omega* 2024, 9, 13051−13058

Read Online

ACCESS | Metrics & More | Article Recommendations | Supporting Information

ABSTRACT: The sodium-rich solid electrolyte, Na_3SO_4F (NSOF), holds promise for eco-friendly and resource-abundant energy storage. While the introduction of heterovalent dopants has the potential to enhance its suitability for battery applications by creating Na vacancies, the effect of vacancies and sodium concentrations on sodium conduction remains unclear. In this work, Mg^{2+} was introduced into Na^+ sites in Na_3SO_4F, generating sodium vacancies with different contents by using solid-state synthesis method. Among the resulting materials, $Na_{2.96}Mg_{0.02}SO_4F$ exhibited an ionic conductivity that is two-order-of-magnitude higher than NSOF at 298 K. Notably, as the sodium concentration decreased, the ionic conductivity also declined, revealing an equilibrium between Na vacancies and concentrations. To further investigate the influence of sodium concentration, excess Na^+ was introduced into $NaMgSO_4F$, which inherently possesses a lower sodium content by using solid-state synthesis method. However, this adjustment only led to an approximately one-order-of-magnitude enhancement in optimal ionic conductivity at 298 K. Combined with an *in situ* X-ray diffraction analysis, our findings underscore the greater sensitivity of sodium conduction to variations in sodium vacancies. This study paves the way for the development of ultrafast sodium ion conductors, offering exciting prospects for advanced energy storage solutions.

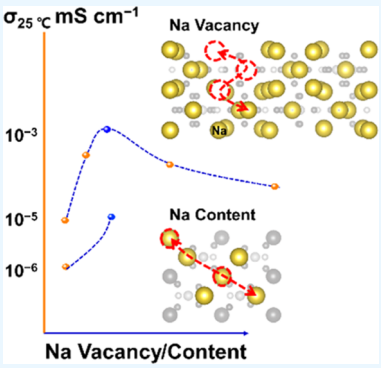

1. INTRODUCTION

Conventional liquid electrolytes present several challenges in battery applications, such as electrode reactions that result in dendrite formation, decreased battery life, and safety hazards including fires and explosions.[1−5] In addition, liquid electrolytes are prone to leakage, causing environmental pollution.[6−9] In comparison to lithium, sodium is a more attractive resource because of its abundance, accessibility, and low cost.[10−15] Therefore, developing sodium solid electrolytes with high ionic conductivity is essential for energy storage and new battery systems.[8,16−18] Recent studies have highlighted the potential correlation between the anion dynamics and cation diffusion properties in solid electrolytes. For example, the disordered rotation of polyanions at elevated temperatures can trigger the "paddle-wheel" mechanism,[19−23] thereby enhancing the ionic conductivity. Therefore, researchers have focused on sodium solid electrolytes containing polyanions[24] like Na_3SO_4F (NSOF). NSOF has a monoclinic structure with a space group $P2_1/m$,[25] as illustrated in Figure 1a. The crystal structure of NSOF contains 13 distinct Na^+ sites, each with coordination numbers ranging from 6 to 8.

Despite its potential, the ionic conductivity of NSOF remains relatively low ($\sim 10^{-8}$ S cm^{-1}[26]), necessitating improvement for practical applications and further development. Common methods to enhance ionic conductivity include adjusting the carrier concentration, improving the phase purity/density, and enhancing the transport channel size and thermal excitation.[27] It is well-known that sodium vacancies, which are responsible for most sodium defects, cause ion transport in sodium-rich solid electrolytes.[17] Generally, higher-valent cations like Al^{3+}, Ca^{2+}, and Mg^{2+} are doped into the Na^+ site to maintain a potential equilibrium, thereby promoting vacancy creation.[28] Codoping with Mg^{2+} and Cl^- has been identified as a promising strategy for increasing the ionic conductivity of NSOF according to the research.[26] In a prior study, our research group assessed the phase stability and conduction properties of Na_3SO_4F and $Na_{2.98}Mg_{0.01}SO_4F$ through experimental analyses, BVSE calculations, and Raman spectroscopy results.[29] We found that SO_4^{2-} does not contribute to the paddle-wheel effect of Na^+ migration in NSOF and $Na_{2.98}Mg_{0.01}SO_4F$, underscoring the significance of introducing vacancies. However, a direct relationship between ionic conductivity and Na vacancy/concentration in NSOF remains elusive. Furthermore, as vacancy content increases, it inevitably leads to a reduction in

Received: November 28, 2023
Revised: February 4, 2024
Accepted: February 8, 2024
Published: March 5, 2024

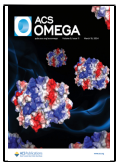

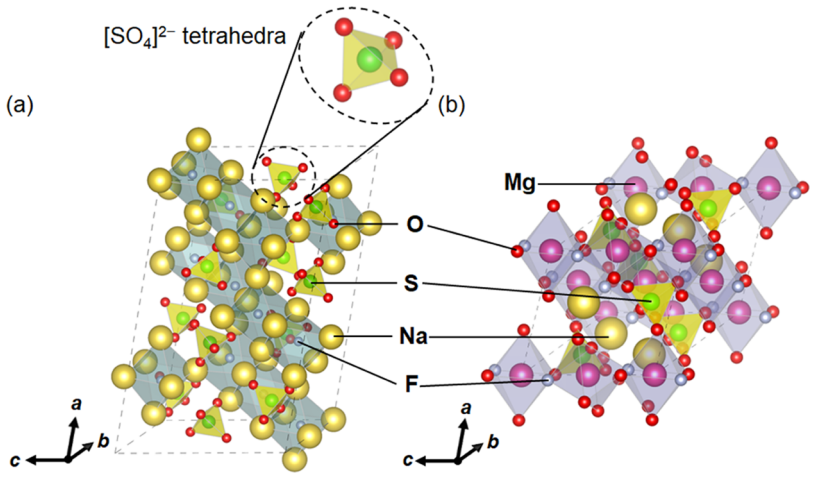

Figure 1. Crystal structures of (a) Na_3SO_4F and (b) $NaMgSO_4F$.

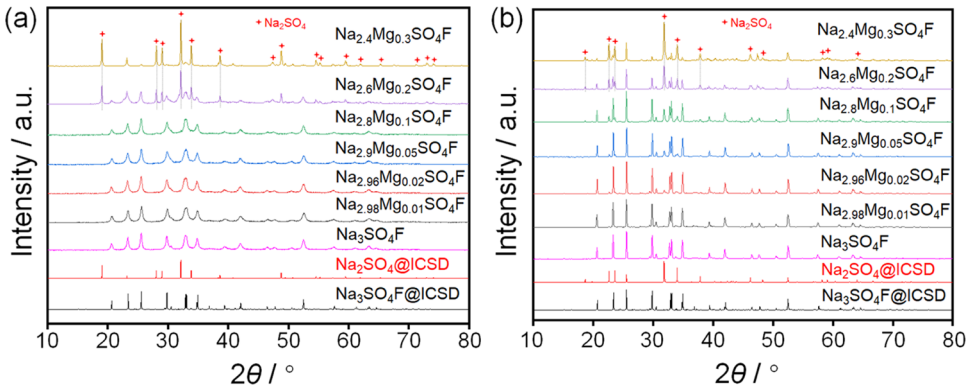

Figure 2. (a) XRD patterns of $Na_{3-2x}Mg_xSO_4F$ ($0 \le x \le 0.3$) prepared after ball milling at 600 r min^{-1} for 20 h. (b) XRD patterns of the compounds obtained were prepared by further sintering the ball-milled $Na_{3-2x}Mg_xSO_4F$ ($0 \le x \le 0.3$) at 580 °C for 24 h. The dotted line indicated the peaks of the impurity Na_2SO_4.

sodium concentration. Therefore, as a comparison experiment, we try to increase the concentration of Na^+ to explore the effect of Na^+ concentration on sodium conduction. However, NSOF is a sodium-rich compound, making it challenging to introduce moveable Na^+ into the lattice. Therefore, a natural monoclinic ore,[30] $NaMgSO_4F$, was employed (Figure 1b). And, $NaMgSO_4F$ exhibits an ionic conductivity of approximately 10^{-10} S cm^{-1} at room temperature (RT, 25 °C).[31]

2. RESULTS AND DISCUSSION

In this work, we explored the relationship between sodium vacancy and ionic conductivity by introducing Mg^{2+} into Na^+ sites to synthesize $Na_{3-2x}Mg_xSO_4F$ ($0 \le x \le 0.3$) via a solid-state synthesis method. The structures and ionic conductivity of these compounds were examined using X-ray diffraction and impedance spectroscopy, respectively. Our results revealed that for compounds with $0 < x \le 0.1$ ($Na_{3-2x}Mg_xSO_4F$), their structure was consistent with NSOF, and the ionic conductivity exhibited remarkable sensitivity to changes in vacancy content. Notably, $Na_{2.96}Mg_{0.02}SO_4F$ exhibited an ionic conductivity of up to 10^{-6} S cm^{-1} at RT, 2 orders of magnitude higher than NSOF. This enhancement can be attributed to a moderate increase in the content of Na vacancies. Subsequently, the ionic conductivity decreases with a decreasing Na^+ concentration. To further verify the effect of Na^+ concentration on sodium ion conduction, Na^+ was introduced into the Mg^{2+} position of $NaMgSO_4F$, which has a limiting sodium content to fabricate $Na_{1+x}Mg_{1-x/2}SO_4F$ ($0 \le x \le 0.4$). Compounds $0 < x \le 0.2$ ($Na_{1+x}Mg_{1-x/2}SO_4F$) exhibit a structure similar to $NaMgSO_4F$, where sodium concentration becomes the predominant factor affecting ionic conductivity. $Na_{1.02}Mg_{0.99}SO_4F$ shows the ionic conductivity of up to 10^{-8} S cm^{-1} at RT, approximately 1 order of magnitude higher than $NaMgSO_4F$.

The solid-state synthesis method used to prepare $NaMgSO_4F$ allowed us to obtain a pure-phase compound with an impressive ionic conductivity of 10^{-9} S cm^{-1} at RT. This conductivity level is approximately 1 order of magnitude higher than the calculated data, which estimated it to be around 10^{-10} S cm^{-1} at RT.[31] The effects of the vacancy mechanism and sodium concentration on sodium conduction were further confirmed by assessing the phase transition temperature of the samples using *in situ* X-ray diffraction. *In situ* Raman spectroscopy was conducted on NSOF and $Na_{2.96}Mg_{0.02}SO_4F$ to determine if SO_4^{2-} experiences significant vibrations at high temperatures, potentially leading to the paddle-wheel effect.

Figure 2a,b shows the XRD patterns of $Na_{3-2x}Mg_xSO_4F$ ($0 \le x \le 0.3$) prepared by the ball milling and further sintering separately. Compared with the standard powder diffraction file card of Na_3SO_4F, all peaks in the patterns confirm the successful synthesis of target compounds. Commonly, the solid-phase sintering method can increase sample density and

https://doi.org/10.1021/acsomega.3c09500
ACS Omega 2024, 9, 13051−13058

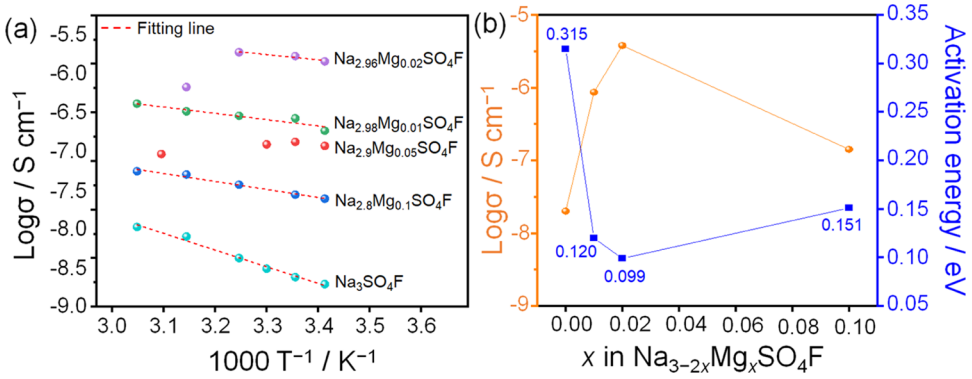

Figure 3. (a) Arrhenius plots of $Na_{3-2x}Mg_xSO_4F$ (x = 0, 0.01, 0.02, 0.05, and 0.1) over a temperature range of 20−55 °C. (b) Composition-dependence plots of the ionic conductivities at 25 °C and activation energy for samples $Na_{3-2x}Mg_xSO_4F$ (x = 0, 0.01, 0.02, and 0.1).

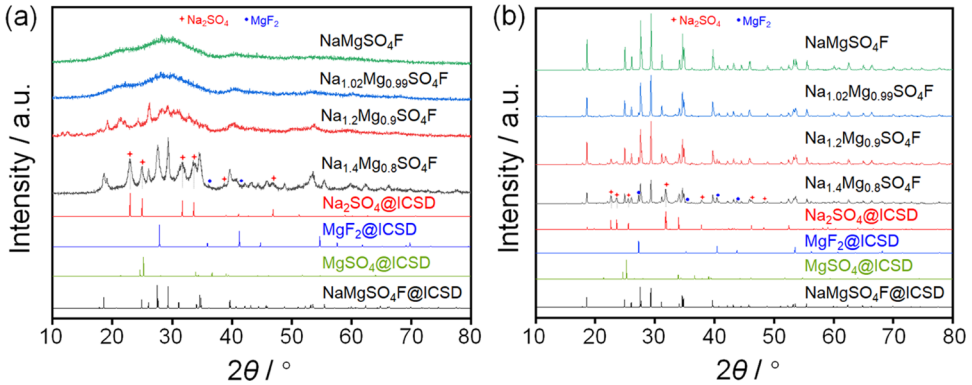

Figure 4. (a) XRD patterns of $Na_{1+x}Mg_{1-x/2}SO_4F$ ($0 \le x \le 0.4$) prepared after ball milling at 600 r min^{-1} for 20 h. (b) XRD patterns of the compounds obtained were prepared by further sintering the ball-milled $Na_{1+x}Mg_{1-x/2}SO_4F$ ($0 \le x \le 0.4$) at 580 °C for 24 h.

crystallinity, thereby reducing grain boundary resistance and enhancing ionic conductivity.[32] Sintering $Na_{2.9}Mg_{0.05}SO_4F$ under the vacuum at various reaction temperatures and durations revealed that the samples obtained at 580 °C for 24 h exhibited fewer impurities compared to other reaction conditions (Figure S1). The impurity of Na_2SO_4 was primarily observed at 2θ = *ca.* 22.7 and 31.8°. Hence, other compounds of $Na_{3-2x}Mg_xSO_4F$ were prepared using this sintering condition. Moreover, Na_3SO_4F exhibited minimal structural changes when exposed to air, confirming its insensitivity to moisture and oxygen (Figure S2). The XRD patterns of $Na_{3-2x}Mg_xSO_4F$ ($0 \le x \le 0.3$) after sintering (Figure 2b) demonstrated the preservation of the monoclinic crystal structure of kogarkoite ore (Na_3SO_4F) with space group $P2_1/m$, even with 10 mol % of Mg doping, indicating that doping did not significantly affect the crystal structure. However, samples with $x > 0.1$ exhibited a complex NSOF-Na_2SO_4 phase, with the intensity ratio of Na_2SO_4 to NSOF increasing as Mg^{2+} concentration increased. Inductively coupled plasma optical emission spectrometry (ICP-OES) was employed to analyze $Na_{2.96}Mg_{0.02}SO_4F$ and determine the cation content. The molar ratio of Na/Mg = 2.94:0.02, close to a theoretical ratio of 2.96:0.02, indicating that the chemical composition was nearly stoichiometric (Table S1).

Figure 3a presents the Arrhenius plots of ionic conductivity of $Na_{3-2x}Mg_xSO_4F$ (x = 0, 0.01, 0.02, 0.05, and 0.1) as a function of temperature. Figure 3b illustrates the relationship between the amount of Mg, ionic conductivity at RT, and the activation energy. After obtaining the data from the linear fit of the Arrhenius plot (Figure 3a), the activation energy (Figure 3b) was calculated according to the Arrhenius equation. The exact calculation process is shown in Section 4. The Nyquist plots of $Na_{3-2x}Mg_xSO_4F$ (x = 0, 0.01, 0.02, 0.05, and 0.1) in the temperature range of 20−55 °C are shown in Figure S3. The structural integrity of both NSOF and $Na_{2.96}Mg_{0.02}SO_4F$ remained unchanged before and after the ionic conductivity testing, indicating the stability of synthesized samples (Figure S4). Typically, thermal agitation due to increased temperature can cause transitions of atoms from their regular lattice sites into interstitial positions, leaving behind lattice vacancies.[33] Thermally activated motion promotes the discrete hopping of atoms from one lattice site to another. First of all, the defect-free compound NSOF was evaluated for ionic conductivity throughout a temperature range of 20−55 °C. Because thermal excitation causes partial point defects in the compound NSOF and facilitates Na^+ transfers across lattice sites, the ionic conductivity of NSOF increases with temperature (Figure 3a). However, the ionic conductivity of Na_3SO_4F at 55 °C is 6.6 × 10^{-8} S cm^{-1}, which is a smaller increase than the ionic conductivity at 25 °C (2.0 × 10^{-8} S cm^{-1}). It further suggests that thermal excitation forms fewer point defects, leading to a small increment in ionic conductivity. Therefore, we next focus on doping high-valent cations to further improve the ionic conductivity.

By replacing part of the Na^+ in the Na_3SO_4F with Mg^{2+}, cation vacancies have to exist to compensate for the excess positive charge of the magnesium. We found that when $0 < x \le 0.1$ ($Na_{3-2x}Mg_xSO_4F$), the structure is close to that of NSOF. And, this method can increase the ionic conductivity of NSOF. Within the range of $0 \le x \le 0.02$, the ionic conductivity

https://doi.org/10.1021/acsomega.3c09500
ACS Omega 2024, 9, 13051−13058

increased significantly with a slight increase in vacancy concentration, indicating a high sensitivity of ionic conductivity to vacancy concentration in this range. Particularly, the compound $Na_{2.96}Mg_{0.02}SO_4F$ with the highest ionic conductivity (up to 3.8×10^{-6} S cm^{-1} at RT) was observed, representing a two-order-of-magnitude enhancement compared to NSOF (2.0×10^{-8} S cm^{-1} at RT). Therefore, the heterovalent doping increases the concentration of vacancies, allowing a series of exchanges between atoms and vacancies. This significantly improves the migration and rearrangement of Na^+ and reduces the activation energy (Figure 3b), thus improving the ionic conductivity of the $Na_{2.96}Mg_{0.02}SO_4F$. However, in the range of $x > 0.02$ ($Na_{3-2x}Mg_xSO_4F$), the ionic conductivity (at RT) gradually decreases, mainly due to the missed optimum equilibrium position between extraneous vacancy and Na^+ concentrations and the increase in the mixed impurity phase.

To further verify the effect of sodium concentration on sodium conduction, we chose $NaMgSO_4F$,[31] which has a limiting sodium content and introduced an excess of Na^+ into its Mg^{2+} position. $Na_{1+x}Mg_{1-x/2}SO_4F$ ($0 \le x \le 0.4$) was prepared using the same optimal synthetic conditions as described above. Figure 4a,b shows the XRD patterns of $Na_{1+x}Mg_{1-x/2}SO_4F$ ($0 \le x \le 0.4$) prepared by the ball milling and further sintering separately. These plots confirmed the preservation of the monoclinic crystal structure of kononovite ore ($NaMgSO_4F$) with space group $C2/c$. However, in the range of $0.2 \le x \le 0.4$, the structure mainly shows the $NaMgSO_4F$–Na_2SO_4–MgF_2 phase with only a negligible presence of $MgSO_4$. This suggests that $Na_{1.2}Mg_{0.9}SO_4F$ has reached its maximum doping limit. According to the Bragg equation, the peak determined by XRD of the compound $Na_{1.02}Mg_{0.99}SO_4F$ shifted to a lower diffraction angle than that of $NaMgSO_4F$, indicating successful doping (Figure 5).

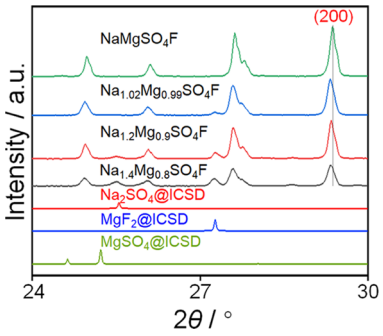

Figure 5. XRD pattern of $Na_{1.02}Mg_{0.99}SO_4F$ shifted to a lower angle than that of the $NaMgSO_4F$.

Temperature-dependent electrochemical impedance spectroscopy was conducted to assess the ionic transport properties of $Na_{1+x}Mg_{1-x/2}SO_4F$ ($0 \le x \le 0.02$) (Figure 6a). Figure 6b shows the relationship between x of the $Na_{1+x}Mg_{1-x/2}SO_4F$ ($x = 0$ and 0.02), ionic conductivity at RT, and activation energy. Nyquist plots of $Na_{1+x}Mg_{1-x/2}SO_4F$ ($x = 0$ and 0.02) in the temperature range of 20–55 °C are presented in Figure S5. We used solid-state synthesis to obtain pure-phase $NaMgSO_4F$ and measured its ionic conductivity data in the laboratory. The solid-state synthesis method yields a purified phase of $NaMgSO_4F$ with an ionic conductivity at least 1 order of magnitude higher (~10^{-9} S cm^{-1} at RT) than the previously calculated ionic conductivity data (~10^{-10} S cm^{-1} at RT).[31] Additionally, the ionic conductivity of $Na_{1.02}Mg_{0.99}SO_4F$ was 5.19×10^{-8} S cm^{-1} at RT, which is approximately 7 times higher than $NaMgSO_4F$ (1.7×10^{-9} S cm^{-1} at RT). This suggests that increasing the concentration of a very slight amount of Na may reduce the activation energy (Figure 6b) and ultimately increase the ionic conductivity.[34] We propose two main reasons for the higher ionic conductivity of $Na_{1.02}Mg_{0.99}SO_4F$ than that of $NaMgSO_4F$. On the one hand, the ionic conductivity σ is proportional to the concentration of mobile carriers (n_c) in the equation $n_c \cdot \exp(-E_a/k_BT)$[35] at a certain temperature. Monovalent alkali metal cations regularly have a higher migration capacity than divalent cations. When low-valent Na^+ is doped into the Mg^{2+} position, the additional sodium ions are compensated, increasing the concentration of migratable sodium ions.[36] On the other hand, since the ionic radius of Na^+ (1.02 Å) is larger than that of Mg^{2+} (0.72 Å), replacing Mg^{2+} with a minimal amount of Na^+ can expand the unit lattice constant and cell volume (Figure 7), improving the ion transport channel bottleneck size and thus reducing the activation energy to increase the ionic conductivity of $Na_{1.02}Mg_{0.99}SO_4F$. Overall, both the vacancy and sodium concentration significantly impact sodium ionic conductivity. However, a low concentration of vacancies ($Na_{2.96}Mg_{0.02}SO_4F$) may prove more effective in enhancing ionic conductivity, underscoring the more significant effect of the vacancy mechanism.

Moreover, Na_3SO_4F undergoes a phase transition between low and high temperatures. After calculating the energy barriers of the Na_3SO_4F distinct phases using the bond valence site energy (BVSE) method, we discovered that the ion migration energy barrier in the high-temperature phase is higher than that in the low-temperature phase, so ions are not prone to movement.[29] In order to further confirm the fact that vacancies are more important for increasing ionic conductivity, *in situ* XRD experiments were conducted on Na_3SO_4F and $Na_{2.96}Mg_{0.02}SO_4F$ within a temperature range of 30–300 °C, with a heating rate of 5 °C/min (Figure 8). Figure 8a,b presents the contour plots of XRD patterns of NSOF and $Na_{2.96}Mg_{0.02}SO_4F$. Phase transition temperatures of NSOF and $Na_{2.96}Mg_{0.02}SO_4F$ were observed at 100 and 45 °C, respectively, with a significant peak cleavage occurring at around 33 and 42°. $Na_{2.96}Mg_{0.02}SO_4F$ having a lower phase transition temperature than NSOF suggests that even a tiny number of Na vacancies can facilitate Na^+ movement, consistent with the higher ionic conductivity of the material. This also explains why the data on the consequent increase in the ionic conductivity of $Na_{2.9}Mg_{0.05}SO_4F$ decreases as the temperature increases.

However, no research has ever demonstrated whether there is a low-temperature–high-temperature phase transition process in $NaMgSO_4F$. Thus, we used this *in situ* XRD technique to make a judgment on its phase transition on $NaMgSO_4F$ and $Na_{1.02}Mg_{0.99}SO_4F$ within a temperature range of 30–440 °C, with a heating rate of 5 °C per minute. Figure 8c shows the contour plot of XRD patterns of $NaMgSO_4F$, while Figure S6a exhibits the XRD pattern of $NaMgSO_4F$ in the temperature range of 30–440 °C. At 230 °C, a new peak appears at 22.6° in $NaMgSO_4F$, and a peak at 39.7° begins to split into two peaks. What's more, the degree of cleavage of the peak at 34.7° deepens with increasing temperature. Figure 8d presents the contour plot of XRD patterns of $Na_{1.02}Mg_{0.99}SO_4F$, and Figure S6b displays the XRD pattern of $Na_{1.02}Mg_{0.99}SO_4F$ between 30 and 440 °C. Besides bearing a

https://doi.org/10.1021/acsomega.3c09500
ACS Omega 2024, 9, 13051–13058

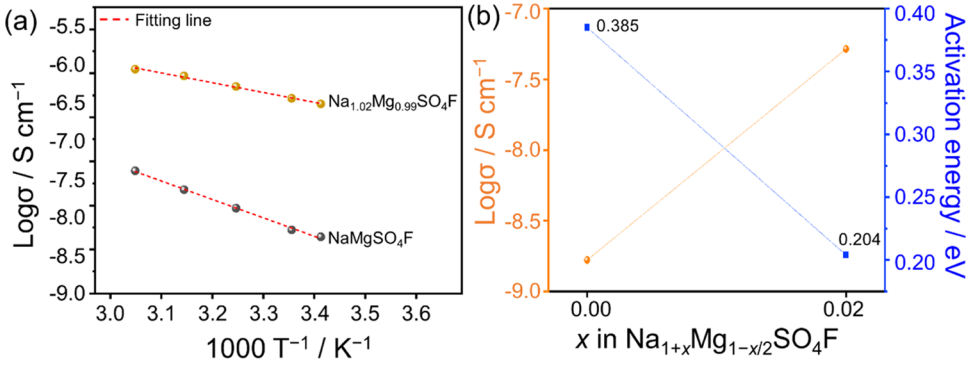

Figure 6. (a) Arrhenius plots of $Na_{1+x}Mg_{1-x/2}SO_4F$ (x = 0 and 0.02) over a temperature range of 20−55 °C. (b) Composition-dependence plot of the ionic conductivities at 25 °C and activation energy for samples $Na_{1+x}Mg_{1-x/2}SO_4F$ (x = 0 and 0.02).

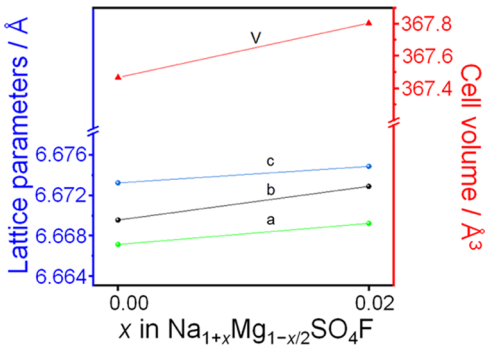

Figure 7. Evolution of the unit lattice parameters and unit-cell volume as a function of the Na-substituted amount in the monoclinic $Na_{1+x}Mg_{1-x/2}SO_4F$ (x = 0 and 0.02).

striking resemblance to the *in situ* XRD results of $NaMgSO_4F$, $Na_{1.02}Mg_{0.99}SO_4F$ exhibits an additional peak of 24.5° at 210 °C. Meanwhile, we found that the above new peaks appearing at certain temperature intervals are neither peaks of the original materials nor peaks of the newly generated substance. However, as the temperature difference in the *in situ* XRD test results was not apparent, we conducted additional thermogravimetry and differential scanning calorimetry (TG-DSC) tests in an argon atmosphere on $NaMgSO_4F$ and $Na_{1.02}Mg_{0.99}SO_4F$ (Figure S7). The results show that there is no heat absorption peak for $NaMgSO_4F$ and $Na_{1.02}Mg_{0.99}SO_4F$ in this temperature range, so there is probably no phase transition for this substance. In other words, it may not be more intuitive to observe the influence of increasing the concentration of Na ions on the migration of sodium ions in

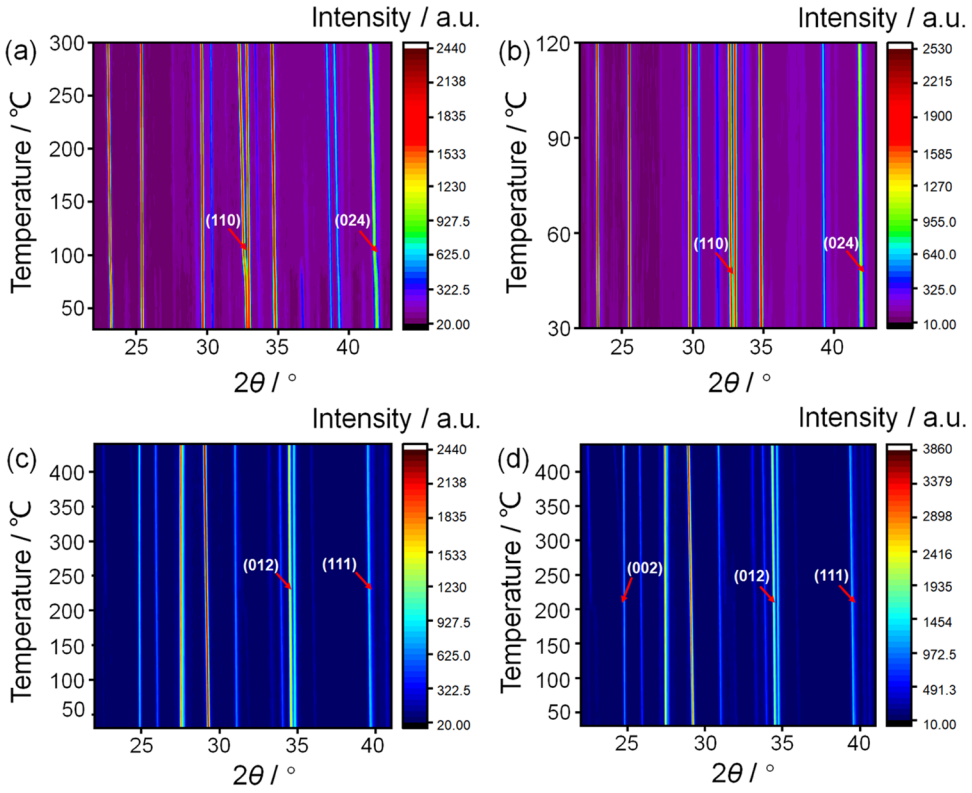

Figure 8. (a) Contour plot of XRD patterns of NSOF from 30 to 300 °C. (b) Contour plot of XRD patterns of $Na_{2.96}Mg_{0.02}SO_4F$ from 30 to 120 °C. (c) Contour plot of XRD patterns of $NaMgSO_4F$ from 30 to 440 °C. (d) Contour plot of XRD patterns of $Na_{1.02}Mg_{0.99}SO_4F$ from 30 to 440 °C.

https://doi.org/10.1021/acsomega.3c09500
ACS Omega 2024, 9, 13051−13058

$NaMgSO_4F$ using the *in situ* XRD technique. In a word, it further validates that a modest increase in vacancy concentration has a greater effect on ion mobility than a modest increase in sodium ion concentration.

Afterward, we evaluated NSOF and $Na_{2.96}Mg_{0.02}SO_4F$ using this *in situ* Raman spectroscopy technique[29] to determine whether the polyanion SO_4^{2-} rotates at high temperatures (Figure S8). The v_1 mode (symmetric stretching vibration) and v_2 mode (bending vibration) are located at wavelengths of 997 and 467 cm^{-1}, respectively, while the v_4 mode (bending vibration)[37] is located in the wavelength range of 622−646 cm^{-1}. If the polyanion rotates with increasing temperature, then the v_2 and v_4 spectral lines will broaden. However, our results show almost no rotation of the polyanion SO_4^{2-} in $Na_{2.96}Mg_{0.02}SO_4F$, suggesting that the paddle-wheel effect is insignificant in ionic conductivity.

3. CONCLUSIONS

In summary, a solid-state synthesis method was applied to synthesize $Na_{3-2x}Mg_xSO_4F$ ($0 \le x \le 0.3$) and $Na_{1+x}Mg_{1-x/2}SO_4F$ ($0 \le x \le 0.4$) to explore the impact of the vacancy mechanism and Na^+ concentration on sodium ion conduction. The ionic conductivity of $Na_{3-2x}Mg_xSO_4F$ ($0 < x \le 0.02$) is highly sensitive to changes in vacancy concentration. $Na_{2.96}Mg_{0.02}SO_4F$ demonstrated the highest ionic conductivity of 3.80×10^{-6} S cm^{-1} at 298 K, which is 2 orders of magnitude higher than that of NSOF. To examine the effect of sodium ion concentration, we found that the ionic conductivity of $Na_{1.02}Mg_{0.99}SO_4F$ with a slight Na^+ doping increased only 7 times compared to $NaMgSO_4F$ at 298 K. It was confirmed that the introduction of a suitable content of vacancies could substantially reduce the temperature of the phase transition, suggesting that vacancies are more likely to significantly improve Na^+ migration. Both solid electrolytes offer the advantages of good air stability, easy synthesis, and low cost, thus providing new and potential candidates for future research on all-solid-state sodium batteries.

4. EXPERIMENTAL SECTION

4.1. Synthesis. Starting materials, including Na_2SO_4 (99.95%), NaF (99.99%), MgF_2 (99.8%), and $MgSO_4$ (98%), were used for the synthesis of $Na_{3-2x}Mg_xSO_4F$ ($0 \le x \le 0.3$) and $Na_{1+x}Mg_{1-x/2}SO_4F$ ($0 \le x \le 0.4$). Na_2SO_4 and NaF were used for the synthesis of NSOF. Na_2SO_4, NaF, and MgF_2 were used as the precursors to obtain $Na_{3-2x}Mg_xSO_4F$ ($0 < x \le 0.3$). $MgSO_4$ and NaF were used to synthesize $NaMgSO_4F$. Na_2SO_4, NaF, and $MgSO_4$ were used to synthesize $Na_{1+x}Mg_{1-x/2}SO_4F$ ($0 < x \le 0.4$). The reagents were mixed in stoichiometric proportions with a total weight of 1 g and ground for 10 min in an agate mortar. The mixture was then milled in a planetary ball mill apparatus (Fritsch Pulverisette 7) using ZrO_2 (ρ = 10 g cm^{-3}) balls at 600 rpm min^{-1} for 20 h in an Ar-filled glovebox with O_2 and H_2O levels below 0.1 ppm. The combined powders were compressed into pellets, sealed in evacuated Pyrex tubes, and sintered for 12−36 h at temperatures between 500 and 580 °C to explore the best sintering condition. Finally, all ball-milled samples were sintered at an optimum temperature of 580 °C for 24 h to form the products.

4.2. Characterization. On a Bruker D8 ADVANCE diffractometer, X-ray diffraction measurements were conducted using Cu Kα radiation at a scanning rate of 1° min^{-1} (2θ = 10 to 80°) at room temperature and operating conditions of 40 mA and 40 kV for the X-ray tube current and voltage, respectively. Samples were placed in the quartz glass sample stage. Using a Bruker D8 ADVANCE diffractometer with an Anton Paar HTK-1200N environmental and temperature control stage, the phase transition of NSOF, $NaMgSO_4F$, $Na_{2.96}Mg_{0.02}SO_4F$, and $Na_{1.02}Mg_{0.99}SO_4F$ was examined. In a corundum (Al_2O_3) sample crucible, samples were fixed. In the temperature range of 30−440 °C, various substances' X-ray profiles were gathered in increments of 10 °C. The time-averaged heating rates were 5 °C min^{-1}. The diffractometer was set up with Cu Kα radiation at 40 kV and 40 mA. Continuous scanning was used to capture the diffraction patterns, with steps of 0.02 from 10 to 80° in 2θ. Raman spectra were collected from the Raman microscope (Renishaw inVia Qontor) using a 532 nm laser. In the LINKAM TS1500 V stage, high-temperature Raman observations were performed up to 320 °C, with the laser output power maintained between 20 and 50 mW for measurements outside and inside the heating stage. The VESTA software[38] drew the plots of the crystal structure. Chemical compositions for Na-loss and Mg-loss tests were performed using inductively coupled plasma optical emission spectrometry (ICP-OES, Thermo Fisher iCAP PRO). The unit-cell parameters were calculated using the software package TOPAS V.6.0 (Bruker DIFFRAC.-SUITE). The thermal behavior of $NaMgSO_4F$ and $Na_{1.02}Mg_{0.99}SO_4F$ was checked by the thermogravimetry and differential scanning calorimetry (TG-DSC, Netzsch STA449-F5) in an argon atmosphere from 30 to 440 °C at a heating rate of 10 °C min^{-1}.

4.3. Ionic Conductivity. The as-synthesized powders were determined using an alternating current (a.c.) impedance spectroscopy to measure ionic conductivity. In a polyether-etherketone (PEEK) die, sample powders were cold-pressed into pellets with diameters of 12 mm and thicknesses of 1 mm. Two stainless steel rods (diameters of 12 mm) were fastened on either side of the sample to act as current collectors. During the electrochemical impedance spectroscopy (EIS) measurements, the die with gaskets was sufficiently hermetic to shield the sample from air and humidity. On the CHI760e, EIS measurements were conducted with an a.c. voltage amplitude of 30 mV and frequencies varying from 0.5 Hz to 0.1 MHz between 20 and 55 °C. After obtaining the data from the Nyquist plots (Figures S3 and S5), the ionic conductivity was calculated using the following equation[39]

$$\sigma = \frac{L}{RS}$$

where σ is the ionic conductivity, L is the thickness of the samples after pelleting, S is the area of the samples after pelleting, and R is the resistance of the measured samples. The value of the thickness of the solid electrolyte material was measured by a vernier caliper. The thickness varies according to the weight of the material and is typically 0.6 mm.

After obtaining the data from the linear fit of the Arrhenius plot (Figure 3a), the activation energy (Figures 3b and 5b) was calculated according to the Arrhenius equation[40]

$$\sigma T = A\, e^{-E_a/kT}$$

where A is the pre-exponential factor, E_a is the activation energy for ionic conduction, k is the Boltzmann constant, and T is the Kelvin temperature.

https://doi.org/10.1021/acsomega.3c09500
ACS Omega 2024, 9, 13051−13058

■ ASSOCIATED CONTENT

Supporting Information

The Supporting Information is available free of charge at https://pubs.acs.org/doi/10.1021/acsomega.3c09500.

X-ray diffraction patterns of $Na_{2.9}Mg_{0.05}SO_4F$ under different synthesis conditions (Figure S1); X-ray diffraction patterns of Na_3SO_4F exposure to air (Figure S2); Nyquist plots of $Na_{3-2x}Mg_xSO_4F$ (x = 0, 0.01, 0.02, 0.05, and 0.10) obtained at different temperatures (Figure S3); X-ray diffraction patterns of Na_3SO_4F and $Na_{2.96}Mg_{0.02}SO_4F$ after ionic conductivity measurements at different temperatures (Figure S4); Nyquist plots of $Na_{1+x}Mg_{1-x/2}SO_4F$ (x = 0 and 0.02) obtained at different temperatures (Figure S5); XRD patterns of $NaMgSO_4F$ and $Na_{1.02}Mg_{0.99}SO_4F$ from 30 to 440 °C (Figure S6); TG and DSC curves of $NaMgSO_4F$ and $Na_{1.02}Mg_{0.99}SO_4F$ obtained at a heating rate of 10 °C min^{-1} between 30 and 440 °C (Figure S7); *in situ* Raman spectra of Na_3SO_4F and $Na_{2.96}Mg_{0.02}SO_4F$ (Figure S8); and metal element content in $Na_{2.96}Mg_{0.02}SO_4F$ (Table S1) (PDF)

■ AUTHOR INFORMATION

Corresponding Authors

Wenqian Chen − *Key Laboratory of Organic Compound Pollution Control Engineering (MOE), School of Environmental and Chemical Engineering, Shanghai University, Shanghai 200444, China*; orcid.org/0000-0001-7946-8957; Email: wenqianchen@shu.edu.cn

Pengcheng Wu − *Department of Chemistry, College of Sciences, Shanghai University, Shanghai 200444, China*; Email: wupengcheng@shu.edu.cn

Liang Tang − *Key Laboratory of Organic Compound Pollution Control Engineering (MOE), School of Environmental and Chemical Engineering, Shanghai University, Shanghai 200444, China*; Email: tang1liang@shu.edu.cn

Authors

Xue Wang − *Key Laboratory of Organic Compound Pollution Control Engineering (MOE), School of Environmental and Chemical Engineering, Shanghai University, Shanghai 200444, China*

Xuele Xu − *Key Laboratory of Organic Compound Pollution Control Engineering (MOE), School of Environmental and Chemical Engineering, Shanghai University, Shanghai 200444, China*

Yuxiang Li − *Department of Chemistry, College of Sciences, Shanghai University, Shanghai 200444, China*

Guowei Zhao − *College of Chemistry and Chemical Engineering, Huanggang Normal University, Huanggang 438000 Hubei, China*; orcid.org/0000-0002-4344-3923

Heng Wang − *Department of Chemistry, College of Sciences, Shanghai University, Shanghai 200444, China*

Ya Tang − *Department of Chemistry, College of Sciences, Shanghai University, Shanghai 200444, China*; orcid.org/0000-0002-3825-7309

Complete contact information is available at: https://pubs.acs.org/10.1021/acsomega.3c09500

Author Contributions

‖X.W. and X.X. contributed equally to this work.

Notes

The authors declare no competing financial interest.

■ ACKNOWLEDGMENTS

The authors gratefully appreciate the financial support provided by the National Natural Science Foundation of China (Nos. 12104286, 22002086, 51803116, and 22201170), the Shanghai Sailing Program (21YF1413300), and the Hubei Provincial Natural Science Foundation Outstanding Youth Fund (No. 2021HG01).

■ REFERENCES

(1) Jana, A.; García, R. E. Lithium Dendrite Growth Mechanisms in Liquid Electrolytes. *Nano Energy* **2017**, *41*, 552−565.

(2) Armand, M.; Tarascon, J.-M. Building Better Batteries. *Nature* **2008**, *451* (7179), 652−657.

(3) Li, W.; Dahn, J. R.; Wainwright, D. S. Rechargeable Lithium Batteries with Aqueous Electrolytes. *Science* **1994**, *264* (5162), 1115−1118.

(4) Singh, R.; Kumari, P.; Kumar, M.; Ichikawa, T.; Jain, A. Implementation of Bismuth Chalcogenides as an Efficient Anode: A Journey from Conventional Liquid Electrolyte to an All-Solid-State Li-Ion Battery. *Molecules* **2020**, *25* (16), No. 3733.

(5) Zhang, L.; Liu, Y.; You, Y.; Vinu, A.; Mai, L. NASICONs-type Solid-state Electrolytes: The History, Physicochemical Properties, and Challenges. *Interdiscip. Mater.* **2023**, *2* (1), 91−110.

(6) Campanella, D.; Belanger, D.; Paolella, A. Beyond Garnets, Phosphates and Phosphosulfides Solid Electrolytes: New Ceramic Perspectives for All Solid Lithium Metal Batteries. *J. Power Sources* **2021**, *482*, No. 228949.

(7) Zhu, F.; Islam, M. S.; Zhou, L.; Gu, Z.; Liu, T.; Wang, X.; Luo, J.; Nan, C.-W.; Mo, Y.; Ma, C. Single-Atom-Layer Traps in a Solid Electrolyte for Lithium Batteries. *Nat. Commun.* **2020**, *11* (1), No. 1828.

(8) Kim, J.-J.; Yoon, K.; Park, I.; Kang, K. Progress in the Development of Sodium-Ion Solid Electrolytes. *Small Methods* **2017**, *1* (10), No. 1700219.

(9) Wang, M.; Wang, Q.; Ding, X.; Wang, Y.; Xin, Y.; Singh, P.; Wu, F.; Gao, H. The Prospect and Challenges of Sodium-ion Batteries for Low-temperature Conditions. *Interdiscip. Mater.* **2022**, *1* (3), 373−395.

(10) Nitta, N.; Wu, F.; Lee, J. T.; Yushin, G. Li-Ion Battery Materials: Present and Future. *Mater. Today* **2015**, *18* (5), 252−264.

(11) Gu, Z.; Guo, J.; Zhao, X.; Wang, X.; Xie, D.; Sun, Z.; Zhao, C.; Liang, H.; Li, W.; Wu, X. High-ionicity Fluorophosphate Lattice via Aliovalent Substitution as Advanced Cathode Materials in Sodium-ion Batteries. *InfoMat* **2021**, *3* (6), 694−704.

(12) Wang, M.; Qin, B.; Wu, S.; Li, Y.; Liu, C.; Zhang, Y.; Zeng, L.; Fan, H. Interface Ion-Exchange Strategy of MXene@$FeIn_2S_4$ Hetero-Structure for Super Sodium Ion Half/Full Batteries. *J. Colloid Interface Sci.* **2023**, *650*, 1457−1465.

(13) Huang, Z.-X.; Zhang, X.-L.; Zhao, X.-X.; Lü, H.-Y.; Zhang, X.-Y.; Heng, Y.-L.; Geng, H.; Wu, X.-L. Suppressing Oxygen Redox in Layered Oxide Cathode of Sodium-Ion Batteries with Ribbon Superstructure and Solid-Solution Behavior. *J. Mater. Sci. Technol.* **2023**, *160*, 9−17.

(14) Qin, B.; Wang, M.; Wu, S.; Li, Y.; Liu, C.; Zhang, Y.; Fan, H. Carbon Dots Confined Nanosheets Assembled $NiCo_2S_4$@CDs Cross-Stacked Architecture for Enhanced Sodium Ion Storage. *Chin. Chem. Lett.* **2023**, No. 108921.

(15) Gu, Z.-Y.; Heng, Y.-L.; Guo, J.-Z.; Cao, J.-M.; Wang, X.-T.; Zhao, X.-X.; Sun, Z.-H.; Zheng, S.-H.; Liang, H.-J.; Li, B.; Wu, X.-L. Nano Self-Assembly of Fluorophosphate Cathode Induced by Surface Energy Evolution towards High-Rate and Stable Sodium-Ion Batteries. *Nano Res.* **2023**, *16* (1), 439−448.

(16) Pan, H.; Hu, Y.-S.; Chen, L. Room-Temperature Stationary Sodium-Ion Batteries for Large-Scale Electric Energy Storage. *Energy Environ. Sci.* **2013**, *6* (8), 2338−2360.

(17) Zhu, J.; Wang, Y.; Li, S.; Howard, J. W.; Neuefeind, J.; Ren, Y.; Wang, H.; Liang, C.; Yang, W.; Zou, R.; Jin, C.; Zhao, Y. Sodium Ion Transport Mechanisms in Antiperovskite Electrolytes Na_3OBr and Na_4OI_2 : An *in Situ* Neutron Diffraction Study. *Inorg. Chem.* **2016**, *55* (12), 5993−5998.
(18) Li, C.; Li, R.; Liu, K.; Si, R.; Zhang, Z.; Hu, Y. NaSICON: A Promising Solid Electrolyte for Solid-state Sodium Batteries. *Interdiscip. Mater.* **2022**, *1* (3), 396−416.
(19) Wiench, D. M.; Jansen, M. Über Na_3PO_4: Versuche zur Reindarstellung, Kristallstruktur der Hochtemperaturform. *Z. Anorg. Allg. Chem.* **1980**, *461* (1), 101−108.
(20) Zhang, Z.; Nazar, L. F. Exploiting the Paddle-Wheel Mechanism for the Design of Fast Ion Conductors. *Nat. Rev. Mater.* **2022**, *7* (5), 389−405.
(21) Kvist, A.; Bengtzelius, A. Tracer Diffusion and Electrical Conductivity of Cubic Lithium Sulphate and a Transport Model for Cubic Sulphates. *Fast Ion Transp. Solids* **1973**, 193−199.
(22) Lundén, A. Evidence for and against the Paddle-Wheel Mechanism of Ion Transport in Superionic Sulphate Phases. *Solid State Commun.* **1988**, *65* (10), 1237−1240.
(23) Gao, L.; Zhang, H.; Wang, Y.; Li, S.; Zhao, R.; Wang, Y.; Gao, S.; He, L.; Song, H.-F.; Zou, R.; Zhao, Y. Mechanism of Enhanced Ionic Conductivity by Rotational Nitrite Group in Antiperovskite Na_3ONO_2. *J. Mater. Chem. A* **2020**, *8* (40), 21265−21272.
(24) Benrath, A.; Drekopf, K. Über die elektrische Leitfähigkeit von Salzen und Salzgemischen. *Z. Phys. Chem.* **1921**, *99U* (1), 57−70.
(25) Žáček, V.; Rapprich, V.; Šíma, J.; Škoda, R.; Laufek, F.; Legesa, F. Kogarkoite, $Na_3(SO_4)F$, from the Shalo Hot Spring, Main Ethiopian Rift: Implications for F-Enrichment of Thermal Groundwater Related to Alkaline Silicic Volcanic Rocks. *J. Geosci.* **2015**, 171−179.
(26) Fan, S.; Lei, M.; Wu, H.; Hu, J.; Yin, C.; Liang, T.; Li, C. A Na-Rich Fluorinated Sulfate Anti-Perovskite with Dual Doping as Solid Electrolyte for Na Metal Solid State Batteries. *Energy Storage Mater.* **2020**, *31*, 87−94.
(27) Zheng, J.; Perry, B.; Wu, Y. Anti-perovskite Superionic Conductors: A Critical Review. *ACS Mater. Au* **2021**, *1* (2), 92−106.
(28) Goldmann, B. A.; Clarke, M. J.; Dawson, J. A.; Islam, M. S. Atomic-Scale Investigation of Cation Doping and Defect Clustering in the Anti-Perovskite Na_3OCl Sodium-Ion Conductor. *J. Mater. Chem. A* **2022**, *10* (5), 2249−2255.
(29) Li, Y.; Wang, X.; Wang, H.; He, T.; Ye, D.; Zhao, H.; Zhao, G.; Zhang, J.; Tang, Y. Unraveling the Dominance of Structural Vacancies in Sodium Ion Conductivity in Na_3SO_4F. *J. Phys. Chem. Lett.* **2023**, *14*, 6832−6839.
(30) Pekov, I. V.; Krzhizhanovskaya, M. G.; Yapaskurt, V. O.; Belakovskiy, D. I.; Chukanov, N. V.; Lykova, I. S.; Sidorov, E. G. Kononovite, $NaMg(SO_4)F$, a New Mineral from the Arsenatnaya Fumarole, Tolbachik Volcano, Kamchatka, Russia. *Eur. J. Mineral.* **2015**, *27* (4), 575−580.
(31) Reynaud, M.; Barpanda, P.; Rousse, G.; Chotard, J.-N.; Melot, B. C.; Recham, N.; Tarascon, J.-M. Synthesis and Crystal Chemistry of the $NaMSO_4F$ Family (M = Mg, Fe, Co, Cu, Zn). *Solid State Sci.* **2012**, *14* (1), 15−20.
(32) DeWees, R.; Wang, H. Synthesis and Properties of NaSICON-Type LATP and LAGP Solid Electrolytes. *ChemSusChem* **2019**, *12* (16), 3713−3725.
(33) Frenkel, J. Über die Wärmebewegung in festen und flüssigen Körpern. *Z. Phys.* **1926**, *35* (8−9), 652−669.
(34) Emly, A.; Kioupakis, E.; Van der Ven, A. Phase Stability and Transport Mechanisms in Antiperovskite Li_3OCl and Li_3OBr Superionic Conductors. *Chem. Mater.* **2013**, *25* (23), 4663−4670.
(35) He, X.; Zhu, Y.; Mo, Y. Origin of Fast Ion Diffusion in Super-Ionic Conductors. *Nat. Commun.* **2017**, *8* (1), No. 15893.
(36) Wang, C.; Sun, Z.; Zhao, Y.; Wang, B.; Shao, C.; Sun, C.; Zhao, Y.; Li, J.; Jin, H.; Qu, L. Grain Boundary Design of Solid Electrolyte Actualizing Stable All-Solid-State Sodium Batteries. *Small* **2021**, *17* (40), No. 2103819.
(37) Toumi, M.; Mhiri, T.; Bulou, A. Raman Spectroscopic Study of $K_3H(SO_4)_2$ (Phases I and II) Single Crystals. *Vib. Spectrosc.* **2009**, *50* (2), 298−302.
(38) Momma, K.; Izumi, F. VESTA 3 for Three-Dimensional Visualization of Crystal, Volumetric and Morphology Data. *J. Appl. Crystallogr.* **2011**, *44* (6), 1272−1276.
(39) Wang, G.; Liang, Y.; Liu, H.; Wang, C.; Li, D.; Fan, L. Scalable. Thin Asymmetric Composite Solid Electrolyte for High-performance All-solid-state Lithium Metal Batteries. *Interdiscip. Mater.* **2022**, *1* (3), 434−444.
(40) Bachman, J. C.; Muy, S.; Grimaud, A.; Chang, H.-H.; Pour, N.; Lux, S. F.; Paschos, O.; Maglia, F.; Lupart, S.; Lamp, P.; Giordano, L.; Shao-Horn, Y. Inorganic Solid-State Electrolytes for Lithium Batteries: Mechanisms and Properties Governing Ion Conduction. *Chem. Rev.* **2016**, *116* (1), 140−162.

https://doi.org/10.1021/acsomega.3c09500
ACS Omega 2024, 9, 13051−13058